ADVANCED MATERIALS
www.advmat.de

Van der Waals Heterojunction Based Self-Powered Biomimetic Dual-Mode Sensor for Precise Object Identification

Xu He, Xinxu Zhu, Zhaoan Hong, Bicheng Wang, Wenting Hong, Yu Yao, Fapeng Sun, Qian Cai, Gang Xu, and Wei Liu**

The design and fabrication of materials that can concurrently respond to light and gas within the dual-modal recognition domain present a significant challenge due to contradictory structural requirements. This innovative strategy introduces a type-I heterojunction, combining the properties of Sb_2Te_3 and WSe_2 nanosheets, to overcome these obstacles. The heterojunction is prepared through a precise stacking approach to create a single-side barrier on the valence band and a near-zero offset on the conduction band. The resulting Sb_2Te_3/WSe_2 heterojunction demonstrates unparalleled performance, showcasing the best integrated photoelectric and gas sensing performance in a single device to date. Based on the above features, the heterojunction successfully integrates visual and olfactory sensing performance, achieving the first biomimetic visual-olfactory dual-mode recognition in a single device. This simulation increased the accuracy of distinguishing electric and fuel-powered cars from ≈50% to ≈96%. This work introduces a novel approach to creating efficient, self-powered sensing materials, paving the way for next-generation biomimetic dual-model devices with broad applications in environmental protection, medical care, and other fields.

1. Introduction

The precise identification of objects is essential in fields such as robotic vision, automated manufacturing, and autonomous driving.[1–6] These areas rely on sensors to gather crucial data about objects, including their shape, smell, dimensions, and other attributes.[7–9] However, current sensor technology, which often relies on a single type of stimulus, frequently, falls short in accuracy.[10–14] In contrast, animals integrate various sensory stimuli to enhance recognition accuracy. For example, dogs utilize both vision and smell to accurately identify objects, such as tracking games or recognizing their owners. Inspired by this natural dual-modal perception, the development of sensors that can process different types of stimuli is becoming a significant trend in sensing technology, aiming to achieve better recognition accuracy and robustness.[15–19]

Current dual-modal recognition technology often employs an array of sensors to sense different stimuli.[20–23] However, this strategy faces several obstacles, such as difficulties in signal synchronization, complex data fusion algorithms, low real-time performance, and high costs.[24–26] If a single device with dual-modal recognition performance could be developed, it would significantly improve upon these issues. Nonetheless, designing sensitive materials to respond to different external stimuli needs to meet different requirements, which can be inherently contradictory (**Scheme 1**, top). For example, defects should generally be avoided in photodetecting materials, as they can capture photocarriers and significantly reduce sensitivity.[27–29] Conversely, in gas-sensing materials, surface defect sites are beneficial for gas absorption and often lead to improved gas sensitivity.[30–32] This contradiction makes it challenging to obtain dual-mode sensing material with high sensitivity for both photo and gas detection in a single device.

To address this issue, we construct a carefully designed type-I heterojunction structure that integrates excellent photoelectric and gas detection performance into a single device (Scheme 1, down). Specifically, a significant band offset is introduced in the valence band of this heterojunction to form a single-side barrier, which blocks the transport of hole carriers and effectively reduces dark current, thereby improving the photodetection response.[33] On the other hand, gas sensing in 2D TMD heterojunctions relies on charge-transfer mechanisms induced by gas molecule

X. He, X. Zhu, Z. Hong, B. Wang, W. Hong, Y. Yao, F. Sun, Q. Cai, G. Xu, W. Liu
State Key Lab of Structural Chemistry
Fujian Institute of Research on the Structure of Matter
Chinese Academy of Sciences
Fuzhou, Fujian 350002, P. R. China
E-mail: gxu@fjirsm.ac.cn; liuw@fjirsm.ac.cn

X. He, G. Xu, W. Liu
Fujian Science & Technology Innovation Laboratory for Optoelectronic Information of China
Fuzhou, Fujian 350108, P. R. China

X. Zhu, F. Sun, G. Xu
University of Chinese Academy of Sciences
Beijing 100049, P. R. China

The ORCID identification number(s) for the author(s) of this article can be found under https://doi.org/10.1002/adma.202411121

DOI: 10.1002/adma.202411121

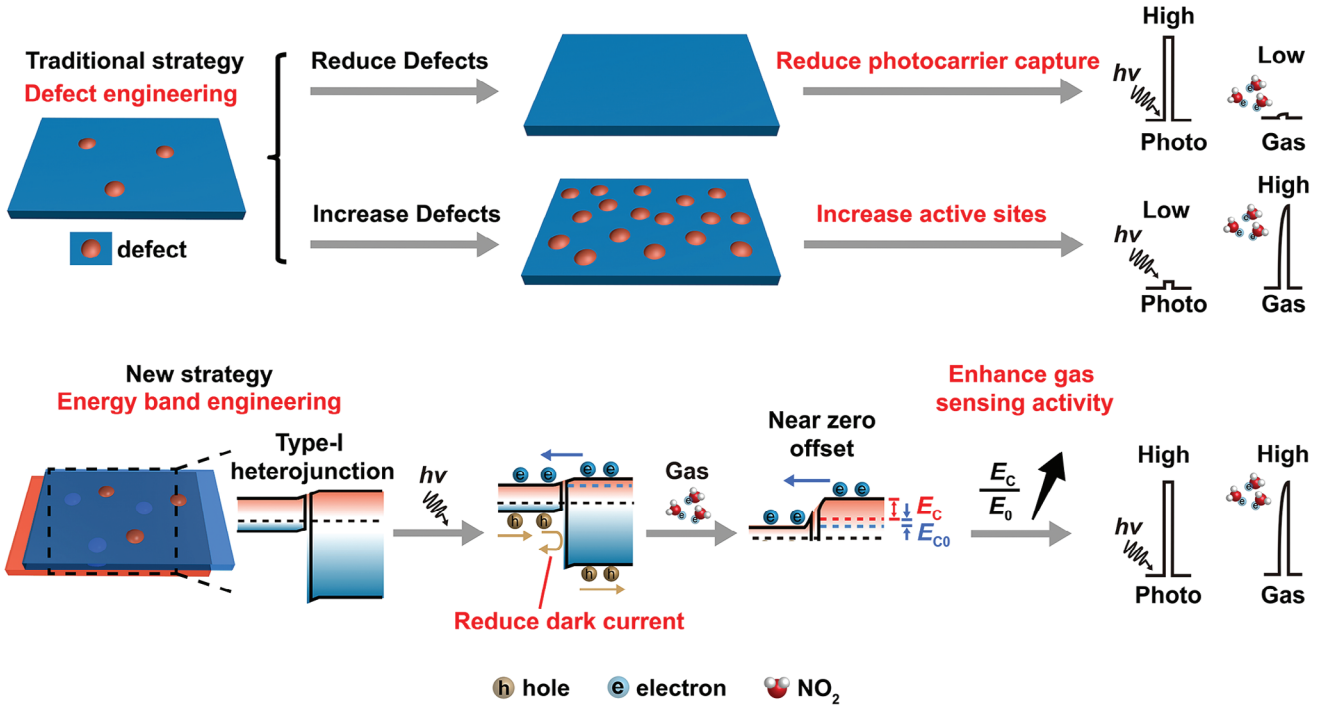

Scheme 1. Scheme illustration of the type-I heterojunction design strategy for high light on/off ratio photodetector and high sensitivity gas sensor in self-powered mode.

adsorption on their surfaces.[34–36] When gases like NO_2 are introduced, they act as electron acceptors, withdrawing electrons from the adjacent layer. This electron withdrawal alters the band structure, changing the device current and enabling gas detection. The response value of the heterojunction positively relates to the ratio of the conduction band offset after and before gas adsorption (E_c/E_{c0}). Accordingly, selecting semiconducting materials with closely aligned conduction band positions for the heterojunction would minimize E_{c0} (near-zero offset). This near-zero offset design is crucial because even slight changes in the conduction band energy level after gas adsorption are significantly amplified when E_{c0} is minimal, enhancing the sensor's sensitivity and selectivity. Consequently, superior photoelectric and gas detection performance are simultaneously realized in a single device.

To validate the feasibility of the aforementioned strategy, we select Sb_2Te_3 and WSe_2 nanosheets to construct a type-I heterojunction featuring a single-side barrier. Interestingly, this heterojunction can realize a desirable self-powered sensor. The Sb_2Te_3/WSe_2 heterojunction exhibits exceptional performance, offering the highest integrated photoelectric and gas sensing performance in a single device reported so far. Based on the exceptionally high-sensing performances, biomimetic vision-olfaction dual-mode sensing is simulated by processing the sensory data from the device and subjecting it to convolutional neural network (CNN) training. This dual-mode detection effectively discerns between electric and fuel-powered cars with identical appearances. The recognition accuracy has been substantially elevated from 50.5%, achievable with single-mode perception, to an impressive 96.4%. This innovation presents a novel paradigm for enhancing the precision and robustness of sensory recognition systems.

2. Results and Discussion

The synthesis of Sb_2Te_3 nanosheets using a Chemical Vapor Deposition (CVD) growth strategy is detailed in the methods section and Figure S1 (Supporting Information). A Transmission Electron Microscopy (TEM) image (Figure S2, Supporting Information) reveals the morphology of the Sb_2Te_3 nanosheets and confirms its single-crystal feature aligning with the (1120) plane.[37] Energy Dispersive X-ray Spectroscopy (EDS) measurements suggest the Sb:Te ratio is 2:3, verifying the high quality of the Sb_2Te_3 crystal. The synthesized Sb_2Te_3 nanosheets are transferred onto a SiO_2/Si substrate using a wet transfer method. WSe_2 nanosheets, mechanically exfoliated from bulk crystals, are subsequently placed atop Sb_2Te_3 using a PDMS-based transfer technique. The resulting heterojunction device, comprising Cr/Au (5/50 nm) electrodes on separate Sb_2Te_3 and WSe_2 layers, is shown in Figure S3 (Supporting Information). AFM measurement confirms the thicknesses of Sb_2Te_3 and WSe_2 nanosheets to be ≈20 and 5 nm, respectively (**Figure 1a**; Figure S4, Supporting Information).

Figure 1b displays Raman spectra for each component and the corresponding heterojunction, indicating a high-quality assembly post-wet transfer and exfoliation.[38,39] The PL spectra (Figure 1c) reveal strong excitonic emission ≈776 nm for bare WSe_2. In the Sb_2Te_3/WSe_2 overlap, significant fluorescence quenching suggests effective charge carrier transfer between WSe_2 and Sb_2Te_3, hindering photogenerated electron-hole recombination and enhancing non-radiative processes.[40] This indicates efficient charge separation at the heterojunction, vital for improving the performance of the self-powered device.

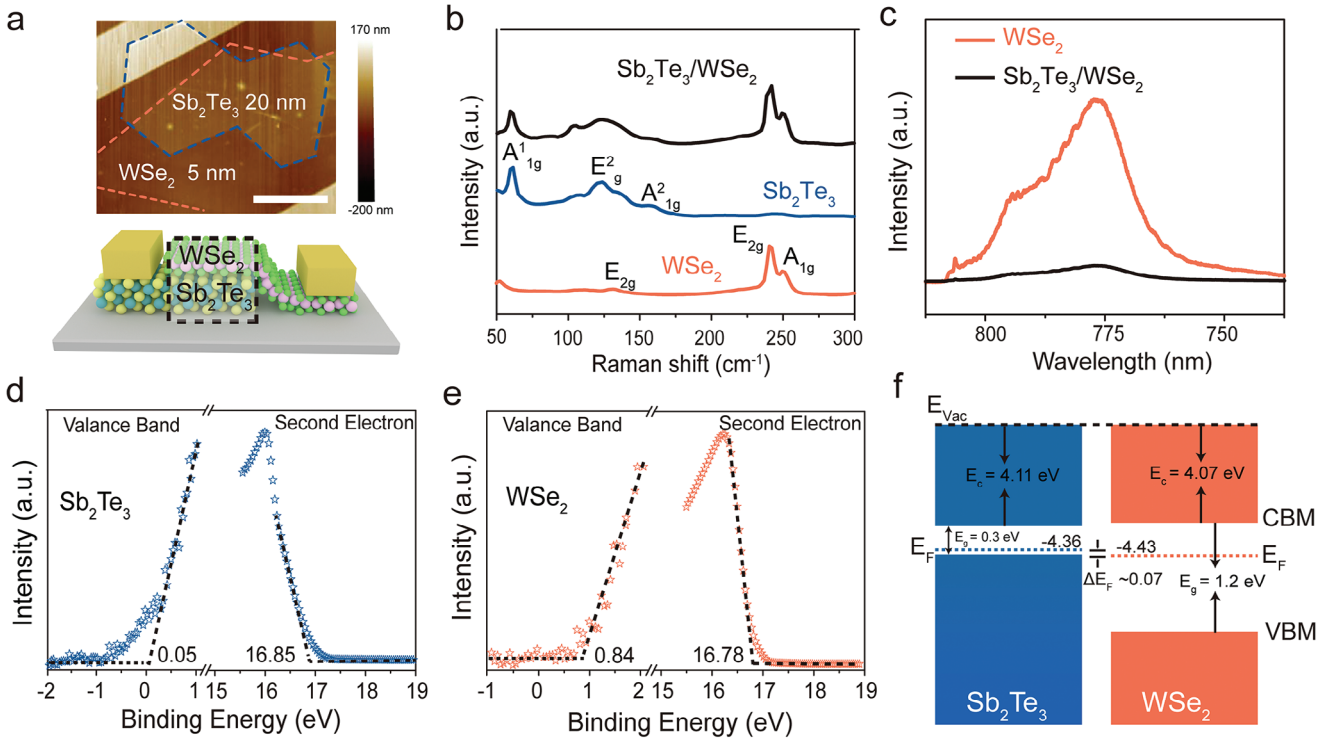

Figure 1. a) Schematic and Atomic Force Microscopy (AFM) image of the Sb_2Te_3/WSe_2 heterojunction device. The scale bar is 10 µm. b) The Raman spectra of WSe_2, Sb_2Te_3, and Sb_2Te_3/WSe_2 heterojunction. c) Photoluminescence (PL) spectra of WSe_2 and the Sb_2Te_3/WSe_2 heterojunction. Ultraviolet photoelectron spectra (UPS) of d) Sb_2Te_3 and e) WSe_2 for the evaluation of work function and valence band edge. f) Schematic of the type-I band diagram of the Sb_2Te_3/WSe_2 heterojunction before contact.

The charge transport behavior in the Sb_2Te_3/WSe_2 heterostructure is governed by its energy band alignment. UPS analysis (Figure 1d,e) reveals the work functions of Sb_2Te_3 and WSe_2 to be 4.36 and 4.43 eV, respectively. The valence band energies of Sb_2Te_3 and WSe_2 are found to be 4.41 and 5.27 eV, respectively.[5] Kelvin probe force microscopy (KPFM) characterization (Figure S5, Supporting Information) indicates a work function difference of ≈70 meV between Sb_2Te_3 and WSe_2, aligning with UPS findings. The transport behaviors and *I*–*V* characteristics of pure Sb_2Te_3 and WSe_2-based field-effect transistors (FETs) reveal their typical p-type and n-type transport behaviors, respectively (Figure S6, Supporting Information), consistent with their band structures.

Considering bandgaps of 0.3 eV for Sb_2Te_3 and 1.2 eV for WSe_2, the band diagrams before contact (Figure 1f) suggest a type-I band alignment.[39,41] The type-I heterojunction construction only allows photogenerated carriers from the wide-bandgap material to pass through, enabling effective modulation of the photocurrent via the wide-bandgap material.[42–44] Therefore, placing the wide-bandgap material on the upper layer in the heterojunction facilitates its adsorption of gas for light-assistant gas sensing. Upon contact (Figure S7a, Supporting Information), electrons diffusion from Sb_2Te_3 to WSe_2 align their Fermi levels, forming a built-in electric field at the interface. Details of the transfer characteristic curve (Figure S7b, Supporting Information) and the corresponding in-depth analysis (Figure S7c, Supporting Information) are provided in the Supporting Information. Meanwhile, a single-side barrier in the valence band of Sb_2Te_3/WSe_2 heterojunction is observed, which can effectively block hole carriers in Sb_2Te_3.[33,44] Consequently, the majority carrier dark current and surface leakage current are blocked by the barrier, leading to a low dark current (<10^{-13} A when $V_{ds} = 0$ V as shown in Figure S8, Supporting Information). In particular, the Sb_2Te_3/WSe_2 heterojunction shows clear current rectification behavior with an ideality factor of 1.32, signifying a quality junction interface.[45]

Figure 2a shows the device's response when exposed to 532 nm light. A key observation is the gradual increase in photocurrent corresponding to rising light power density, attributed to the increased generation of electron-hole pairs under more intense illumination. Under illumination (Figure S9, Supporting Information), the photogenerated holes in WSe_2 are collected by the electrode driven by the built-in electric field. The photogenerated electrons of WSe_2 across the heterointerface, contributing to a short-circuit current (I_{sc}) that evidences the photovoltaic (PV) effect in the heterojunction.[46] On the other hand, the photogenerated holes in Sb_2Te_3 are impeded by the valence band single-side barrier, indicating that the photocurrent in the Sb_2Te_3/WSe_2 heterojunction primarily originates from carriers in WSe_2.[43] The wavelength dependent (635 and 1550 nm) of the vdW Sb_2Te_3/WSe_2 devices are provided in Figures S10 and S11 (Supporting Information). The spectral response shows negligible self-powered property when the device is exposed to 1550 nm light. Since 1550 nm light can only be absorbed by Sb_2Te_3 materials (0.3 eV), this observation confirms that the photogenerated electron-hole pairs in the Sb_2Te_3 side recombine quickly and

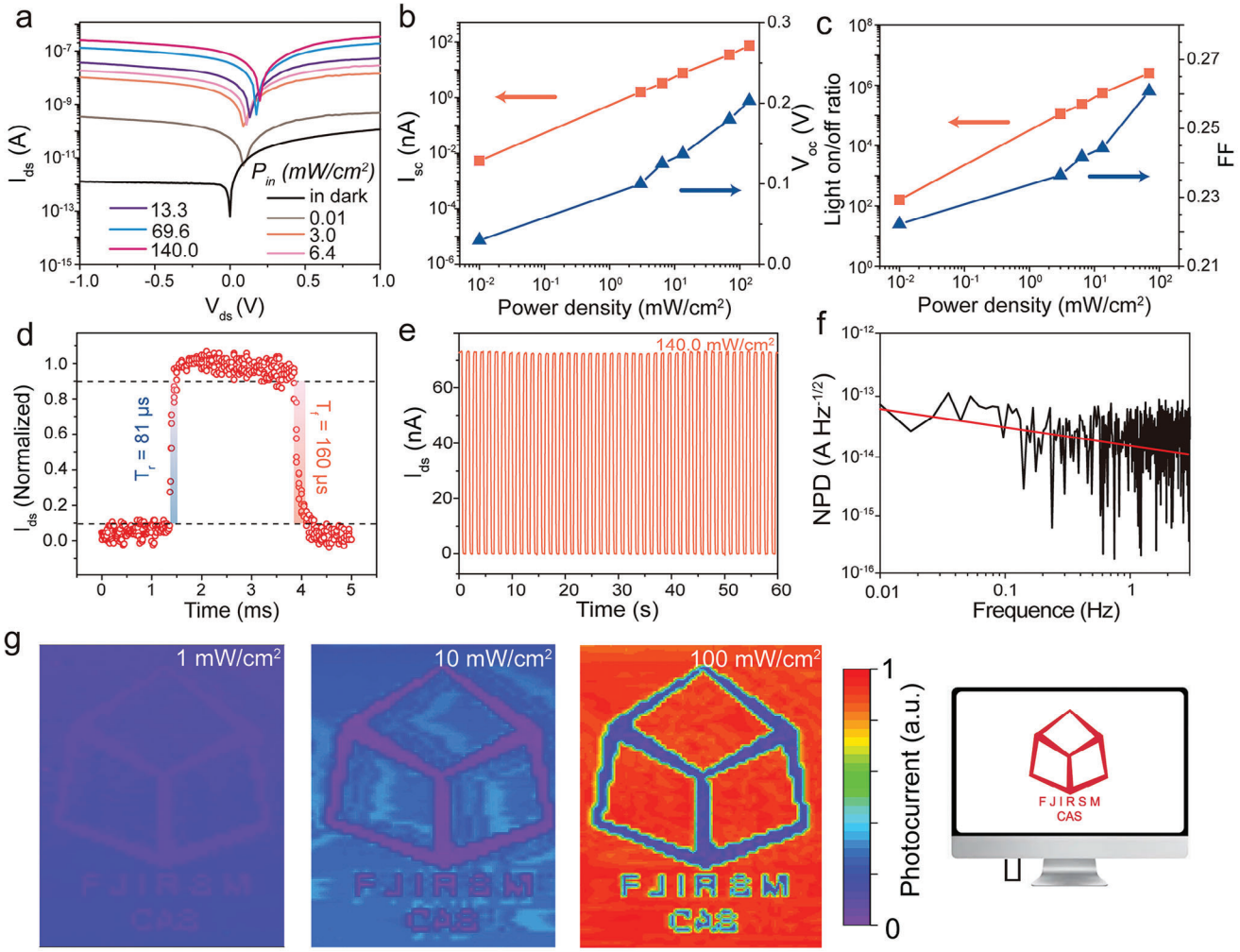

Figure 2. a) The logarithmic-scale I_d-V_d curves of Sb_2Te_3/WSe_2 photodetector under dark and 532 nm laser illumination of various power densities. b) Extracted I_{sc} and V_{oc} under various laser power intensities. c) Light on/off ratio and fill factor (FF) under various laser power intensities at V_d = 0 V. d) The time-resolved photoresponse of the device. e) Photoresponse cycles of the Sb_2Te_3/WSe_2 photodetector. f) Current noise power density spectrum of the Sb_2Te_3/WSe_2 heterojunction photodetector. g) The resulting image obtained with Sb_2Te_3/WSe_2 photodetector at zero-bias under 532 nm light with the light intensities of 1, 10, and 100 mW cm^2, respectively. The use of the abbreviation "FJIRSM" has been approved by the corresponding author's institution.

fail to generate photocurrent, further substantiating that WSe_2 plays a dominant role in the photoresponse of the heterojunction. Extracted I_{sc} and open circuit voltage (V_{oc}) from the enlarged I_d-V_d curves as shown in Figure 2b and Figure S12 (Supporting Information), demonstrates that the I_{sc} increases linearly with the light intensity and V_{oc} exhibits a logarithmic dependence, aligning with the expected behavior of photocurrent variations in PV effects.[47] The electrical power of the device is calculated (Figure S13, Supporting Information), peaking at 3.7 nW at 140 mW cm^2.

Notably, due to the ultra-low dark current (<10^{-13} A), the photoresponse on/off ratio reached 10^6 (Figure 2c), which endows the device with a weak light signal detection capability.[48–50] The maximum fill factor was 0.26. The response speed features a rise time of 81 μs and a fall time of 160 μs (Figure 2d). Time-dependent photocurrent measurements under periodic laser exposure (140 mW cm^2) demonstrated excellent stability and reproducibility (Figure 2e). The photovoltaic responsivity of the device can reach 410 mA W^{-1} at the intensity of 0.01 mW cm^2. The current noise power density spectrum of the Sb_2Te_3/WSe_2 heterojunction device is revealed in Figure 2f. The calculated detectivity of our device is 3.6×10^{10} Jones (all of the formulas are described in Supporting Information). Details of the power intensity-dependent behavior to calculate the linear dynamic range of the vdW Sb_2Te_3/WSe_2 devices is provided in Figure S14 (Supporting Information). These performance metrics are among the best-reported heterojunction photodetectors in self-powered operation, as detailed in Table S1 (Supporting Information).

To showcase the self-powered visual perception capability of the Sb_2Te_3/WSe_2 photodetector, it is used as a single-point sensing pixel in a zero-bias imaging system. An introduction to the single-pixel imaging process is provided in the Supporting Information. The schematic of the measurement setup is displayed in

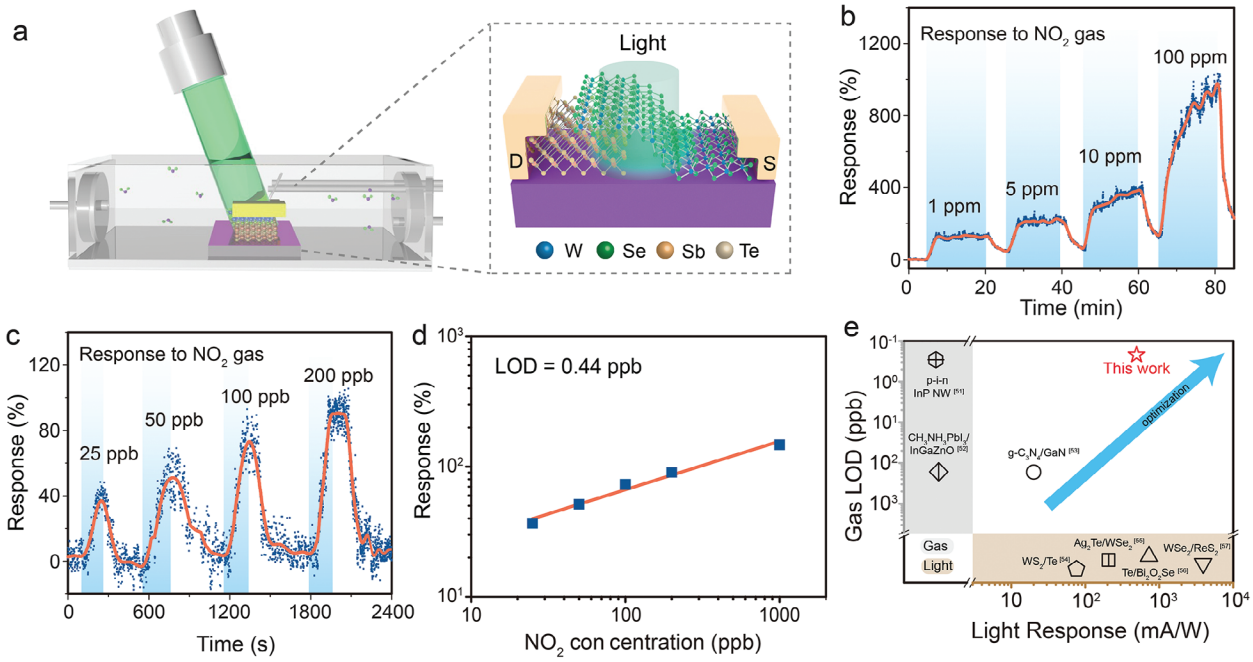

Figure 3. a) Schematic of self-powered home-built gas sensing system under the illumination of the laser. b,c) Sensing response measurement of the device for different ranges of NO_2 concentrations d) Summarized NO_2 concentration (25–1000 ppb) versus calculated response. e) Comparison of gas limit of detection (LOD) and light response among the reported literature. The studies in the gray section exclusively provide gas LOD, while those in the brown section focus solely on light response.[51–57] The sensing measurements are performed under a 532 nm laser with a light intensity of 10 mW cm^2.

Figure S15 (Supporting Information). The images obtained under different light intensities (1, 10, 100 mW cm^2) at zero bias (Figure 2g) demonstrate the device's excellent self-powered visual perception capability, with clear and recognizable imaging results.

The near-zero offset (70 meV) design in the conduction band makes the Sb_2Te_3/WSe_2 heterojunction highly susceptible to the influence of gas absorption. The olfactory perception performance of the specially designed device is assessed by detecting NO_2 using a custom-built gas sensing system (**Figure** 3a). The device's self-powered sensing performance is characterized without any external bias voltage.

To further demonstrate the practicality of the visual-olfactory dual-mode sensor in real-world scenarios, we conducted tests under complex light and color conditions, as well as in the presence of multicomponent gas interference. Specifically, we evaluated the gas response under varying light intensities (Figure S16, Supporting Information) and examined the impact of high-intensity white light on the device's performance during operation (Figure S17, Supporting Information). The experimental results indicate that the dual-mode sensor exhibits strong resistance to light interference. Impressively, the device still exhibits a response of 120% to 1 ppm NO_2 at a reduced light intensity of 1 mW cm^2, ≈1% of the 1-sun condition. This is the highest reported response value for a self-powered NO_2 sensor. As shown in Figure S18 (Supporting Information), the device also exhibits response and recovery times of 107 and 248 s for NO_2, respectively. To evaluate the device's stability, it is repeatedly exposed to 1 ppm NO_2 and a consistent sensing response for an extended period is observed in Figure S19 (Supporting Information). Additionally, we tested the sensor's response to seven commonly encountered interference gases (Figure S20, Supporting Information), confirming that the device selectively responds to NO_2, with no significant interference from other gases. These results affirm the sensor's reliability and practicality.

The concentration-dependent response to NO_2, ranging from 25 ppb to 100 ppm under 10 mW cm^2 532 nm light illumination, is depicted in Figure 3b and c. A gradual increase in sensing response is observed by increasing gas concentration, with substantial recovery achieved after switching back to dry air. Figure 3d demonstrates the high linearity of the response to low-concentration NO_2. The limit of detection (LOD) is determined to be 0.44 ppb (the formula is described in Supporting Information),[51,58] which is currently the lowest reported for self-powered gas sensors.

In Table S2 (Supporting Information), we provide a detailed comparison of our device's sensing performance with other recently reported self-powered gas sensors. Our Sb_2Te_3/WSe_2 gas sensor demonstrates exceptional performance, with high sensitivity (135%/1 ppm), the lowest LOD of 0.44 ppb, and robust functionality independent of light intensity at room temperature. As illustrated in Figure 3e, the Sb_2Te_3/WSe_2 heterojunction demonstrates unparalleled performance, exhibiting the highest integrated photoelectric and gas sensing performance reported thus far. To confirm the repeatability of our devices, we tested seven devices from different batches, all of which demonstrated similar responses (Figure S21, Supporting Information).

The outstanding self-powered visual and olfactory perception performance provide a possibility to improve perception accuracy by vision-olfaction dual-mode recognition, which is demonstrated by simulation tests. Using photoelectric detection data

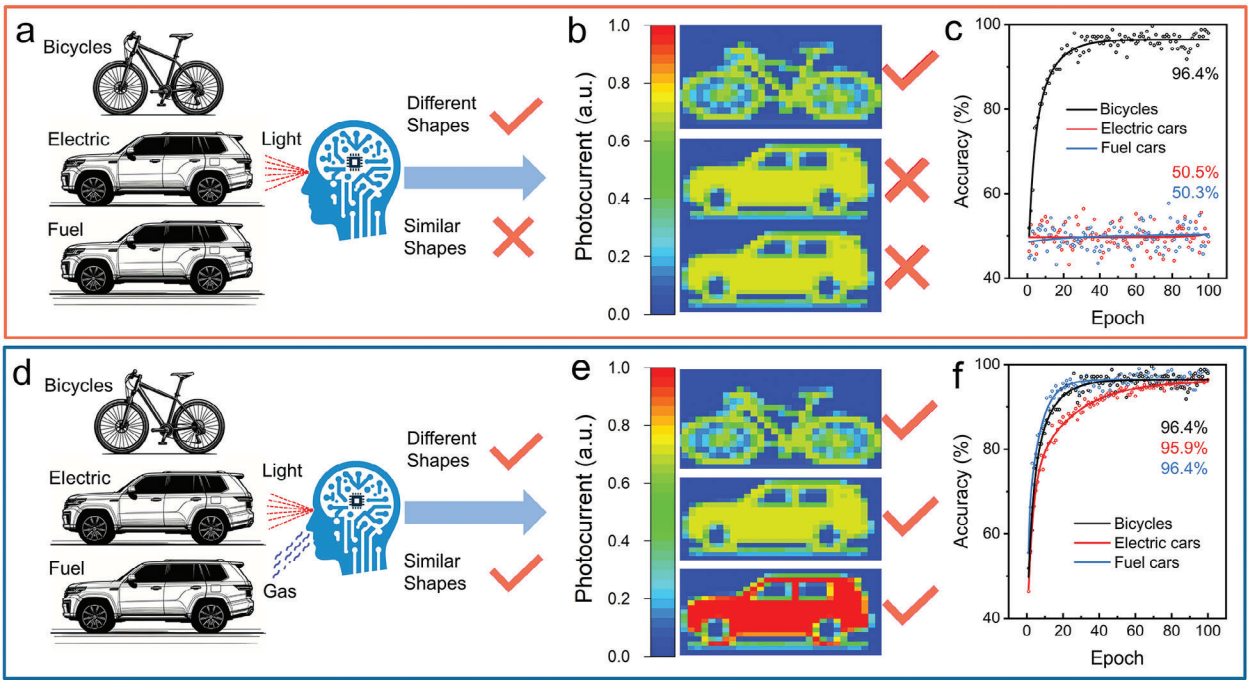

Figure 4. The schematic diagrams for a) visual perception recognition and d) vision-olfaction dual-mode recognition, along with simulated sensory perception images b,e) of bicycles, electric cars, and fuel cars under 10 mW cm^2 light intensity and 1 ppm NO_2 (fuel cars only), and the identification accuracy c,f) obtained through CNN training of detection data.

under different light intensities, single-point imaging data, and self-powered gas-sensitive detection data for different concentrations of NO_2, convolutional neural network calculations are performed to simulate visual recognition and vision-olfaction dual-mode recognition. **Figure** 4a depicts the schematic diagram for visual perception recognition, where bicycles, electric cars, and fuel cars were perceived under a 10 mW cm^2 light intensity. The simulated perception images are illustrated in Figure 4b, demonstrating the device's accurate perception of the external features of the target objects. Furthermore, the device exhibited excellent visual perception performance under different light intensities, as depicted in the simulated perception images in Figure S22 (Supporting Information). Each of the three target objects comprised 50 images used for training, each image consisting of 600 pixels. After training with a convolutional neural network, this resulted in the identification accuracy curve (Figure 4c). The results indicate that visual perception recognition can accurately differentiate between bicycles and cars with different external features, achieving a recognition accuracy of 96.4% for bicycles. However, for electric cars and fuel cars with similar external features, the recognition accuracies were 50.5% and 50.3%, respectively. This suggests that relying solely on visual perception recognition is insufficient to effectively distinguish target objects with similar external features, which is a major challenge in traditional optical recognition.

Combining visual and olfactory information for vision-olfaction dual-mode recognition (Figure 4d) can effectively distinguish objects with similar external features, significantly improving accuracy. Since only fuel cars emit NO_2, an additional 1 ppm of NO_2 was introduced during the simulation for their recognition (Figure 4e). The testing methods are provided in the Supporting Information. Furthermore, effective recognition was achieved within the 1–100 ppm range, with results shown in Figure S23 (Supporting Information). This dual-mode approach combines traditional visual features with gas detection data, enabling the differentiation of objects with similar external features. Additionally, due to the self-powered nature of the device, the olfactory sensing system remains inactive in the absence of light (Figure S24, Supporting Information), preventing any interference with the visual perception imaging. Figure 4f illustrates the identification accuracy after CNN training of vision-olfaction dual-mode perception images. Details of the CNN model are provided in the Supporting Information. The results demonstrate that vision-olfaction perception recognition can accurately differentiate between bicycles and cars with different external features, as well as accurately identify electric cars and fuel cars with similar external features. The recognition accuracies for bicycles, electric cars, and fuel cars were 96.4%, 95.9%, and 96.4%, respectively, surpassing the blind spots of traditional visual recognition and providing a new approach to enhancing the accuracy and robustness of sensor-based recognition.

3. Conclusion

To overcome the contrary structure design requirement in traditional light and gas sensing materials, a type-I heterojunction strategy is proposed for developing a dual-mode sensing material. By strategically stacking the Sb_2Te_3 nanosheet and WSe_2 nanosheet, a Sb_2Te_3/WSe_2 type-I heterojunction is prepared and endowed with a unique single-side barrier on the valence band and near-zero offset on the conduction band. These unique features in band structure remarkably suppress dark current

and promote the response increment for sensing. As a result, this heterojunction showcases the highest reported integrated performance in photoelectric and gas sensing in a single device to date. Furthermore, through integrating visual and olfactory information to construct biomimetic vision-olfaction dual-mode recognition, target objects with similar external features can be effectively distinguished with recognition accuracies increased from ≈50% to ≈96%. This work not only provides a new strategy for designing high-performance, self-powered dual-mode sensing material, but also opens up new horizons for the development of advanced sensor technologies. Looking ahead, we aim to further design the sensing materials to detect a broader range of gases, allowing the visual-olfactory dual-mode sensing system to be applied in a more diverse set of scenarios.

4. Experimental Section

Chemicals: All the materials were purchased from commercial suppliers and used without further purification.

Synthesis of Sb_2Te_3 Nanosheets on the Mica: The Sb_2Te_3 nanosheets were grown on the mica using the CVD method. The Sb_2Te_3 powders and the mica were placed at the center and downstream of the furnace tube, respectively. Before heat, the furnace tube was purged with high-purity argon (Ar) for 5 min to purge the air inside. Then the furnace was heated to 520 °C at a rate of 40 °C min^{-1} and kept for 10 min. Ar flow of 50 sccm was kept during the whole growth process. After the growth, the furnace was cooled naturally to room temperature.

Devices Fabrication: The 2D WSe_2 flakes were obtained by mechanically exfoliating bulk crystals. The as-grown Sb_2Te_3 nanosheets were first transferred on a SiO_2/Si substrate using a PS-assisted wet transfer method. Then, WSe_2 was transferred onto the Sb_2Te_3 nanosheet using a PDMS-based transfer technique. The devices were fabricated using electron-beam lithography to define the electrode pattern and electron beam evaporation to deposit Cr/Au (10/50 nm) contact electrodes on the SiO_2/Si substrates.

Characterization: Optical microscope images were recorded using a Nikon Eclipse microscope. The thicknesses of the Sb_2Te_3 and WSe_2 nanosheets were measured using a Bruker Dimension Icon in ScanAsyst mode with Bruker ScanAsyst-Air probes. Transmission electron microscopy (TEM) characterization was performed using an FEI Titan F20 equipped with an energy dispersive spectroscopy (EDS) system. Raman spectra were collected from the Sb_2Te_3/WSe_2 vdWH using a confocal microscope (HORIBA, LabRAM, HR800) with a 532 nm laser as the excitation source. The photoluminescence spectrum was measured using a microfluorescence spectrometer (Mstarter 100).

Measurements: The electronic and photoelectronic measurements were carried out by a semiconductor characterization system (Hewlett-Packard 4155B) with a multi-wavelength optical-fiber laser on a probe station. The gas sensing tests were performed in a home-built gas sensing system.

Supporting Information

Supporting Information is available from the Wiley Online Library or from the author.

Acknowledgements

X.H. and X.Z. contributed equally to this work. This work was supported by the National Natural Science Foundation of China (Nos. 52202323, 52372240, 22325109, 91961115, 22171263, and 62227815), the Natural Science Foundation of Fujian Province of China (Nos. 2021J05096, 2021J01520, 2023J05074), Scientific Research and Equipment Development Project of CAS (YJKYQ20210024), the Fujian Science & Technology Innovation Laboratory for Optoelectronic Information of China (No. 2021ZR102, 2021ZR101), and and the Self-deployment Project Research Program of Haixi Institutes, Chinese Academy of Sciences, CXZX-2022-GH09.

Conflict of Interest

The authors declare no conflict of interest.

Data Availability Statement

The data that support the findings of this study are available on request from the corresponding author. The data are not publicly available due to privacy or ethical restrictions.

Keywords

2D materials, dual-mode sensor, self-powered, type-I van der Waals heterojunction, ultralow dark current

Received: July 29, 2024
Revised: October 8, 2024
Published online:

[1] Y. Wu, W. Deng, K. Li, X. Wang, B. Liu, J. Li, Z. Chen, Y. Zhang, *Adv. Mater.* **2024**, *36*, 2312094.
[2] X. Zhang, H. Li, Q. Gao, Z. Yuan, S. He, X. Yu, Z. L. Wang, T. Cheng, *Nano Energy* **2023**, *108*, 108239.
[3] L. Chen, K. Yuan, S. Chen, Y. Huang, H. Askari, N. Yu, J. Mo, N. Xu, M. Wu, H. Chen, *Nano Energy* **2023**, *113*, 108575.
[4] T. Zhang, Y. Ding, C. Hu, M. Zhang, W. Zhu, C. R. Bowen, Y. Han, Y. Yang, *Adv. Mater.* **2023**, *35*, 2203786.
[5] N. Zhang, F. Wang, P. Li, Y. Liang, H. Luo, D. Ouyang, L. Luo, J. Wu, Y. Zhao, Y. Li, *Mater. Today* **2023**, *69*, 79.
[6] X. Hong, Y. Huang, Q. Tian, S. Zhang, C. Liu, L. Wang, K. Zhang, J. Sun, L. Liao, X. Zou, *Adv. Sci.* **2022**, *9*, 2202019.
[7] Z. Zheng, H. Li, L. Hai, R. Ma, R. Liu, C. Zhai, Z. Sun, F. Wang, Y. Ma, Q. Xie, *Adv. Funct. Mater.* **2024**, *34*, 2307093.
[8] J. Choi, T. Kim, H. Li, H.-T. Jung, D. Zhao, *ACS Appl. Mater. Interfaces* **2023**, *15*, 44119.
[9] H. Yuan, N. Li, W. Fan, H. Cai, D. Zhao, *Adv. Sci.* **2022**, *9*, 2104374.
[10] J. Xiao, Z. Zhang, S. Wang, C. Gao, L. Wang, *Chem. Eng. J.* **2024**, *479*, 147569.
[11] D. Wang, D. Zhang, J. Guo, Y. Hu, Y. Yang, T. Sun, H. Zhang, X. Liu, *Nano Energy* **2021**, *89*, 106410.
[12] F. Gao, H. Chen, W. Feng, Y. Hu, H. Shang, B. Xu, J. Zhang, C. Y. Xu, P. Hu, *Adv. Funct. Mater.* **2021**, *31*, 2104359.
[13] W. Su, S. Zhang, C. Liu, Q. Tian, X. Liu, K. Li, Y. Lv, L. Liao, X. Zou, *Nano Lett.* **2022**, *22*, 10192.
[14] L. Wang, X. Zou, J. Lin, J. Jiang, Y. Liu, X. Liu, X. Zhao, Y. F. Liu, J. C. Ho, L. Liao, *ACS Nano* **2019**, *13*, 4804.
[15] Z. Wang, T. Wan, S. Ma, Y. Chai, *Nat. Nanotechnol.* **2024**, 1.
[16] J. Liu, W. Zhao, J. Li, C. Li, S. Xu, Y. Sun, Z. Ma, H. Zhao, L. Ren, *Biosens. Bioelectron.* **2024**, *243*, 115773.
[17] H. Wang, Q. Ding, Y. Luo, Z. Wu, J. Yu, H. Chen, Y. Zhou, H. Zhang, K. Tao, X. Chen, *Adv. Mater.* **2024**, *36*, 2309868.
[18] S. Wang, X. Wang, Q. Wang, S. Ma, J. Xiao, H. Liu, J. Pan, Z. Zhang, L. Zhang, *Adv. Mater.* **2023**, *35*, 2304701.

[19] Y. Liu, J. Tao, Y. Mo, R. Bao, C. Pan, *Adv. Mater.* **2024**, 2313857.
[20] K. Keum, J. Y. Kwak, J. Rim, D. H. Byeon, I. Kim, J. Moon, S. K. Park, Y.-H. Kim, *Nano Energy* **2024**, *122*, 109342.
[21] X. Zhi, S. Ma, Y. Xia, B. Yang, S. Zhang, K. Liu, M. Li, S. Li, W. Peiyuan, X. Wang, *Nano Energy* **2024**, *125*, 109532.
[22] J. Zhu, X. Zhang, R. Wang, M. Wang, P. Chen, L. Cheng, Z. Wu, Y. Wang, Q. Liu, M. Liu, *Adv. Mater.* **2022**, *34*, 2200481.
[23] R. Yang, W. Zhang, N. Tiwari, H. Yan, T. Li, H. Cheng, *Adv. Sci.* **2022**, *9*, 2202470.
[24] Z. Huang, S. Yu, Y. Xu, Z. Cao, J. Zhang, Z. Guo, T. Wu, Q. Liao, Y. Zheng, Z. Chen, *Adv. Mater.* **2024**, 2407329.
[25] Y. Du, J. Tang, Y. Li, Y. Xi, Y. Li, J. Li, H. Huang, Q. Qin, Q. Zhang, B. Gao, *Adv. Mater.* **2024**, *36*, 2302658.
[26] Y. Li, J. Long, Y. Chen, Y. Huang, N. Zhao, *Adv. Mater.* **2022**, *34*, 2200517.
[27] Y. Xi, G. Li, T. Ji, Y. Hao, S. Liu, Y. Liu, Y. Cui, *Adv. Funct. Mater.* **2024**, 2407525.
[28] G. Li, S. Li, J. Ahmed, W. Tian, L. Li, *InfoMat* **2024**, e12594.
[29] W. Liu, Y. Yu, M. Peng, Z. Zheng, P. Jian, Y. Wang, Y. Zou, Y. Zhao, F. Wang, F. Wu, *InfoMat* **2023**, *5*, e12470.
[30] N. Sun, Q. Tian, W. Bian, X. Wang, H. Dou, C. Li, Y. Zhang, C. Gong, X. You, X. Du, *Appl. Surf. Sci.* **2023**, *614*, 156213.
[31] K. Sun, G. Zhan, L. Zhang, Z. Wang, S. Lin, *Sens. Actuators, B* **2023**, *379*, 133294.
[32] G. Mathankumar, P. Bharathi, J. Archana, S. Harish, M. Navaneethan, *Sens. Actuators, B* **2022**, *353*, 131057.
[33] Y. Chen, Y. Wang, Z. Wang, Y. Gu, Y. Ye, X. Chai, J. Ye, Y. Chen, R. Xie, Y. Zhou, *Nat. Electron.* **2021**, *4*, 357.
[34] B. Cho, M. G. Hahm, M. Choi, J. Yoon, A. R. Kim, Y. J. Lee, S. G. Park, J. D. Kwon, C. S. Kim, M. Song, Y. Jeong, K. S. Nam, S. Lee, T. J. Yoo, C. G. Kang, B. H. Lee, H. C. Ko, P. M. Ajayan, D. H. Kim, *Sci. Rep.* **2015**, *5*, 8052.
[35] Y. Kim, S. Lee, J. G. Song, K. Y. Ko, W. J. Woo, S. W. Lee, M. Park, H. Lee, Z. Lee, H. Choi, W. H. Kim, J. Park, H. Kim, *Adv. Funct. Mater.* **2020**, *30*.
[36] C. Zhou, W. Yang, H. Zhu, *J. Chem. Phys.* **2015**, *142*, 214704.
[37] S. Singh, S. Kim, W. Jeon, K. P. Dhakal, J. Kim, S. Baik, *Carbon* **2019**, *153*, 164.
[38] X. He, L. Zhang, W. Hong, B. Wang, F. Sun, Z. Hong, Q. Cai, Z. Sun, W. Liu, *Adv. Opt. Mater.* **2023**, *11*, 2300319.
[39] H. Liu, D. Li, C. Ma, X. Zhang, X. Sun, C. Zhu, B. Zheng, Z. Zou, Z. Luo, X. Zhu, *Nano Energy* **2019**, *59*, 66.
[40] K. Xiao, S. Zhang, K. Zhang, L. Zhang, Y. Wen, S. Tian, Y. Xiao, C. Shi, S. Hou, C. Liu, *Adv. Sci.* **2024**, 2401716.
[41] P. Luo, F. Wang, J. Qu, K. Liu, X. Hu, K. Liu, T. Zhai, *Adv. Funct. Mater.* **2021**, *31*, 2008351.
[42] L. Meng, Y. Li, B. Yao, Z. Ding, G. Yang, R. Liu, R. Deng, L. Liu, *J. Appl. Phys.* **2016**, 120.
[43] J. Liu, Q. Hao, H. Gan, P. Li, B. Li, Y. Tu, J. Zhu, D. Qi, Y. Chai, W. Zhang, *Laser Photonics Rev.* **2022**, *16*, 2200338.
[44] F. Wu, Q. Li, P. Wang, H. Xia, Z. Wang, Y. Wang, M. Luo, L. Chen, F. Chen, J. Miao, *Nat. Commun.* **2019**, *10*, 4663.
[45] S. Chen, Y. Fu, M. Ishaq, C. Li, D. Ren, Z. Su, X. Qiao, P. Fan, G. Liang, J. Tang, *InfoMat* **2023**, *5*, e12400.
[46] X. Hu, X. Li, G. Li, T. Ji, F. Ai, J. Wu, E. Ha, J. Hu, *Adv. Funct. Mater.* **2021**, *31*, 2011284.
[47] D. J. Groenendijk, M. Buscema, G. A. Steele, S. Michaelis de Vasconcellos, R. Bratschitsch, H. S. van der Zant, A. Castellanos-Gomez, *Nano Lett.* **2014**, *14*, 5846.
[48] F. Sun, W. Hong, X. He, C. Jian, Q. Ju, Q. Cai, W. Liu, *Small* **2023**, *19*, 2205353.
[49] M. Kumar, S. Lim, J. Kim, H. Seo, *Adv. Mater.* **2023**, *35*, 2210907.
[50] R. Gherabli, S. Indukuri, R. Zektzer, C. Frydendahl, U. Levy, *Light Sci. Appl.* **2023**, *12*, 60.
[51] S. Wei, Z. Li, K. Murugappan, Z. Li, F. Zhang, A. G. Saraswathyvilasam, M. Lysevych, H. H. Tan, C. Jagadish, A. Tricoli, *Adv. Mater.* **2023**, *35*, 2207199.
[52] M. T. Vijjapu, S. G. Surya, J.-H. He, K. N. Salama, *ACS Appl. Mater. Interfaces* **2021**, *13*, 40460.
[53] M. Reddeppa, N. T. KimPhung, G. Murali, K. S. Pasupuleti, B.-G. Park, I. In, M.-D. Kim, *Sens. Actuators, B* **2021**, *329*, 129175.
[54] Z. Luo, H. Xu, W. Gao, M. Yang, Y. He, Z. Huang, J. Yao, M. Zhang, H. Dong, Y. Zhao, Z. Zheng, J. Li, *Small* **2023**, *19*, 2207615.
[55] F. Sun, W. Hong, X. He, C. Jian, Q. Ju, Q. Cai, W. Liu, *Small* **2023**, *19*, 2205353.
[56] W. Wang, Y. Meng, W. Wang, Z. Zhang, P. Xie, Z. Lai, X. Bu, Y. Li, C. Liu, Z. Yang, *Adv. Funct. Mater.* **2022**, *32*, 2203003.
[57] A. Varghese, D. Saha, K. Thakar, V. Jindal, S. Ghosh, N. V. Medhekar, S. Ghosh, S. Lodha, *Nano Lett.* **2020**, *20*, 1707.
[58] K. Wu, M. Debliquy, C. Zhang, *Chem. Eng. J.* **2022**, *444*, 136449.